Direct determination of momentum-resolved electron transfer in the photoexcited van der Waals heterobilayer WS_2/MoS_2

Fang Liu, Qiuyang Li, X.-Y. Zhu*

Department of Chemistry, Columbia University, New York, NY 10027, USA

ABSTRACT

Photo-induced charge separation in transition metal dichalcogenide heterobilayers is being explored for moiré excitons, spin-valley polarization, and quantum phases of excitons/electrons. While different momentum spaces can be critically involved in charge separation dynamics, little is known directly from experiments. Here we determine momentum-resolved electron dynamics in the WS_2/MoS_2 heterobilayer using time and angle resolved photoemission spectroscopy (TR-ARPES). Upon photoexcitation in the *K* valleys, we detect electrons in *M*/2, *M*, and *Q* valleys/points on time scales as short as ~70 fs, followed by dynamic equilibration in *K* and *Q* valleys in ~400 fs. These findings reveal the essential role of phonon scattering, the coexistence of direct and indirect interlayer excitons, and constraints on spin-valley polarization.

Monolayer transition metal dichalchogenides (TMDCs) are excellent models for the exploration of semiconductor physics at the two-dimensional (2D) limit, with potential applications in electronics, optoelectronics, and quantum devices [1]. Heterobilayers formed from stacking two TMDC monolayers may bring about new physical properties or processes, such as moire excitons [2–4], long-lived spin valley polarization [5,6], exciton condensation [7,8], and quantum phases of carriers [9]. For TMDC heterobilayers with type-II band alignment, photoexcitation of one monolayer leads to electron or hole transfer to the other layer, resulting in interlayer excitons with electron and hole spatially separated across the interface. Interlayer excitons have been characterized in photoluminescence spectroscopies, and the corresponding interlayer charge transfer is evidenced in transient absorption/reflectance spectroscopies and THz emission [9–16]. It has been found that photoinduced interlayer charge transfer occurs on ultrafast

* To whom correspondence should be addressed. E-mail: xyzhu@columbia.edu

(<100 fs) time scales, regardless of relative layer orientation [13,14,17,18]. This observation is surprising since the conduction band (CB) minimum and valence band (VB) maximum are both located at the K/K' points at the hexagonal Brillouin zone corners, and relative orientation between the two monolayers should result in momentum mismatch. A likely mechanism for efficient charge transfer involves phonon-assisted scattering of photoexcited CB electrons from the K valleys of one monolayer to other energetically resonant momentum regions [10,19]. However, experimental evidences for such momentum-indirect interlayer charge transfer and the roles of optically dark interlayer excitons are absent at the present time.

In contrast to optical experiments, time and angle resolved photoemission spectroscopy (TR-ARPES) enables direct characterization of dynamics in the momentum space. TR-ARPES experiments have been used to reveal photoexcited electron dynamics and band renormalization in TMDC monolayers with femtosecond time resolution. [20–23] Here we apply TR-ARPES for the first time to probe electron transfer mechanisms in a single-crystal and single-domain TMDC heterobilayer, $MoSe_2/WSe_2$, with time, energy, and momentum resolutions. Recently, Wilson et al. applied micro-ARPES to probe the static valence band structure of the $MoSe_2/WSe_2$ heterobilayer, This study revealed strong hybridization of valence bands from the two monolayers at the Γ point [24] but cannot provide dynamic information on the charge transfer process. In comparison, our TR-ARPES determines the dynamics of ultrafast distribution of CB electrons across the Brillouin zone in the heterobilayer following across gap photoexcitation. Specifically, TR-ARPES measurements will (i) solve a major mystery in the field – the insensitivity of ultrafast charge separation to interlayer twist angle in TMDC heterobilayers; (ii) reveal the dominant role of phonon scattering is mediating interlayer electron transfer; and (iii) identify the presence of a dynamic equilibrium between optically bright K-K (K'-K') excitons with the optically dark K(K')-Q excitons in angle-aligned heterobilayers.

The pump-probe scheme of the TR-ARPES is shown in Fig. 1a. The visible pump ($h\nu_1$ = 2.2 eV, 40 fs pulse width, s-polarized, 0.5-2 mJ/cm^2, spot diameter 0.5-1 mm) excites electrons from VB to CB, and the extreme UV probe (EUV, $h\nu_2$ = 22 eV, pulse duration <100 fs, 10 kHz, p-polarized, ~10^9 photons/s, spot diameter 200 μm) ionizes the electrons from both valence and conduction bands after a controlled time delay for detection by a hemispherical analyzer. We used a WS_2/MoS_2 heterobilayer with lateral size > 3 mm (image shown in Fig. 1b and Fig. S1 [25]) and

a small interlayer twist angle of 5° as determined by second harmonic generation (SHG, Fig. S2 [25]). The sample is prepared from a gold-tape exfoliation technique [26] on a dielectric substrate (285 nm thick SiO_2 on n-doped Si) to minimize disturbance to the electronic properties [20]. Gold electrodes are deposited on the side for grounding. The SHG mapped across the heterobilayer area for TR-ARPES measurements (Fig. 1c) shows uniform phase, reflecting the homogeneous single crystal quality and the uniform crystal orientation of the heterobilayer sample.

Fig. 1(d) shows predicted band structure of the angle-aligned WS_2/MoS_2 heterobilayer from first principle calculation by Okada et al [27]. Wavefunctions at the K/K' point band edges are strongly confined within each monolayer, with little interlayer electronic interaction [19,27,28]. In contrast, Γ point of the VB, Q and the $M/2$ valleys of the CB have significant mixed characters of both monolayers [19,29]. The EUV probe-only photoionization ARPES maps out the valence band structure for the WS_2/MoS_2 heterobilayer along Γ-K and Γ-M directions, as shown in Fig. 1d and 1e, which agrees with the theoretical prediction. The band structure of heterobilayer and the corresponding energy distribution curves (EDCs) is compared with those from the monolayer WS_2 and MoS_2, showing hybridization at the Γ point from monolayer bands compared with K point (Fig. S3 - S4 [25]), in agreement with that found in high resolution static valence band ARPES of $MoSe_2/WSe_2$ heterobilayers [24].

We carry out pump probe TR-ARPES measurements around five representative positions in the momentum space, including the Brillouin zone center Γ, corner K (K'), edge M and the halfway positions of Q and $M/2$. Fig. 2 shows the ARPES of CB without ($\Delta t < 0$) and with ($\Delta t = 0$) visible pump excitation, with the EDCs shown in the bottom panel. The monolayers are intrinsically n-doped. [20,30–32] The intrinsic electron doping population is observed close to the Fermi level (E_F) at $\Delta t < 0$ predominantly near the K point, which is predicted to be the global CB minimum. When the pump pulse overlaps with the probe pulse at $\Delta t = 0$, the conduction band electron population increases at K, Q, M and $M/2$ positions. The initial pump pulse induces direct transition in the K valleys in both WS_2 and MoS_2 monolayers, as known from the much larger oscillator strength of intralayer excitons than that of the interlayer [33]. Observation of CB electrons at the other momentums near $\Delta t = 0$ indicates ultrafast intervalley scattering upon the initial excitation. The CB electrons are not observable at Γ, which is predicted at higher energy.

The integrated CB electron intensities at the *K*, *Q*, *M*, and *M*/2 are recorded as a function of Δt, shown in Fig. 3. The corresponding energy-resolved 2D pseudo-color plots are shown in Fig. S5. The *M* and *M*/2 CB electron population undergo a sharp rise followed by fast decay to zero. We fit the *M* and *M*/2 dynamics using an instantaneous rise with a single exponential decay, convoluted with Gaussian function (black curve in Fig. 3, detailed in supplementary information). The variance of the convoluting Gaussian, $\sigma = 140 \pm 30$ fs, represents an estimated upper limit in experimental time constant of ~70 fs ($^1/_2\ \sigma$). It indicates that interlayer electron transfer from the *K* to *M*/2 and *M* occur with a time constant of $\tau_M \leq 70$ fs. The *M*/2 position has strong interlayer electronic coupling, which is also energetically close to initial *K* valley excitation of WS_2. Following the ultrafast rise, the electron populations decay with single exponential lifetime of $\tau_{Md} = 0.7\pm0.1$ ps at both *M* and *M*/2. As we discuss below, this decay can be attributed to the transfer of electron population to the lower-lying *Q* (mixed WS_2 and MoS_2) and *K* (MoS_2) valleys, Auger recombination, as well as other nonradiative charge recombination channels.

In contrast to the fast formation and decay of *M*/2 and *M* electrons, CB electron signal at *Q* or *K* in Fig. 3 has a delayed feature. The kinetics can be fit with two components, including a prompt formation from initial excitation ($\tau_{r1} \leq 70$ fs) and the delayed formation ($\tau_{r2} = 0.6\pm0.3$ ps) which may be attributed to inter-valley back scattering from *M* and *M*/2. The initial prompt formation dominates the kinetics at *K*, while the delayed formation component with $\tau_{r2} = 0.6\pm0.3$ ps is more significant in *Q*. Following the rise, the decay of *Q* and *K* electrons can be described by bi-exponentials, with time constants for the fast and slow channels of $\tau_{d1} = 0.7$-1.7 ps and $\tau_{d2} \geq 40$ ps. The fast channel is likely a result of many body scattering, such as Auger recombination at the initial high excitation density. The slow decay channel is assigned to the radiative and nonradiative recombination of direct and indirect interlayer excitons, respectively. The majority of CB electrons reside at the *K* point, which is predicted to be the global conduction band minimum. The *Q* point lies close in energy (see Fig. 1a, energy offset discussed in the SI). The similarity in the kinetic profiles at longer times reveals a dynamic equilibrium of CB electrons at the *K* and *Q* points. The CB electrons at *K* and *Q* points form optically bright *K*-*K* (*K*′-*K*′) and the dark *K*(*K*′)-*Q* excitons, respectively, with holes located at *K*(*K*′).

The dominant dynamic pathways following photoexcitation of the WS_2/MoS_2 heterobilayer revealed by TR-ARPES is summarized in Fig. 4. Following the initial cross-gap excitation at *K*,

the CB electrons quickly occupy a broad momentum space covering the *K*, *Q*, *M* and *M*/2 positions within ≤ 70 fs time scale, likely from efficient phonon scattering known in 2D TMDCs [19,34]. In contrast to the layer localized *K* valleys, the CB at *Q* and *M*/2 exhibit significant hybridization from wavefunctions of both monolayers, [19,29] facilitating interlayer charge transfer. Subsequently, on time scales of $\tau \sim 0.6$ ps, the CB electrons at the *M*/2 and *M* positions are scattered to the lower energy *K* and *Q* valleys. The CB electrons in the *K* and *Q* valleys undergo recombination with VB holes on longer time scales of ≥ 40 ps. During this time, the bright *K*-*K* (*K′*-*K′*) excitons are in dynamic equilibrium with the dark *K*(*K′*)-*Q* excitons. The momentum conservation in these intervalley scattering processes requires the participation of a phonon, likely a longitudinal optical (LO) phonon, via the efficient Fröhlich scattering mechanism. In most polar semiconductors, Fröhlich scattering occurs on the ultrafast time scale of a few to a few tens femtoseconds [35]. A TR-ARPES study on bulk MoS_2 reveals inter-valley scattering from the initially populated *K* valley to the *Σ* valley in ≤ 50 fs [36], in excellent agreement with the present finding of ultrafast inter-valley scattering in the WS_2/MoS_2 heterobilayer. The strong interlayer electronic coupling at *Q* and *M*/2 valleys and the ubiquitous involvement of LO phonon scattering may explain the ultrafast charge transfer in TMDC heterobilayers regardless of twist angles [10,19].

Although we did not attempt to assign the CB electrons to that of the WS_2 and MoS_2 bands individually due to limited energy resolution, early time dynamics indeed show a relaxation in average electron energy in the *K* valley by ~ 100 meV on the ~0.5-1 ps time scale, as shown in Fig. S6a-b [25]. Such energy relaxation is not detectable in monolayer MoS_2 or the *Q* valleys in the heterobilayer. This energy relaxation may reflect interlayer charge transfer from *K* point of WS_2 to *K* point of MoS_2 (via the *M*/2, *M*, and *Q*) as well as hot electron relaxation.

The result presented above suggest that valley polarization of CB electrons is lost on ultrafast time scales for TMDC heterobilayers. As is shown in Fig. S7 [25], circularly polarized excitations in our TR-ARPES measurement results in equal amounts of CB electrons in the *K* and *K′* valleys. Circularly polarized light achieves spin-valley specific excitation at *K*/*K′* points in monolayer TMDC and heterostructures [37,38]. However, the CB energy splitting of opposite spins are negligible at *K*/*K′* points, resulting in approximately equal probability of electron scattering to *K* and *K′* from the midpoint *M*/2 and *M*. The dynamic equilibrium between *Q* and *K*/*K′* further

scrambles the CB spin-valley polarization. A recent TR-ARPES study of bulk WSe_2 also reveals that CB valley polarization is lost in ~100 fs [39]. In contrast to the CB, spin-orbit energy splitting in VB is an order of magnitude larger (100s meV). Spin polarized hole scattering from K/K' to the opposite K'/K valleys will need to overcome a large energy offset. Therefore, holes in the VB may maintain a high degree of spin-valley polarization. Although unpolarized CB electrons occupy both K/K' valleys, only electrons at the same valley as holes can give rise to optically bright transitions. As a result, spin valley polarized holes may be solely responsible for the circularly polarized light emission/absorption/reflection, as is measured in previous optical spectra [5,6,40]. In such optical spectroscopy measurements, CB electrons at the Q and the spin-opposite $K'(K)$ valleys may act as dark reservoirs, albeit in competition with phonon-assisted radiative or nonradiative recombination. Moreover, confinement of interlayer exciton to the spin-valley polarized $K(K')$ valleys may be assisted by the Moiré potential, provided the excitation density and the temperature are both sufficiently low [2,3].

Acknowledgement

XYZ acknowledges the National Science Foundation (NSF) grant DMR-1809680 for supporting the TR-ARPES experiments on the heterobilayer and grant DMR-1608437 on the monolayers. XYZ acknowledges the Center for Precision Assembly of Superstratic and Superatomic Solids, a Materials Science and Engineering Research Center (MRSEC) through NSF grant DMR-1420634 , the Columbia Nano Initiative and the Vannevar Bush Faculty Fellowship through Office of Naval Research Grant # N00014-18-1-2080 for the purchase of the laser equipment. FL acknowledges support by the Department of Energy (DOE) Office of Energy Efficiency and Renewable Energy (EERE) Postdoctoral Research Award under the EERE Solar Energy Technologies Office administered by the Oak Ridge Institute for Science and Education (ORISE). ORISE is managed by Oak Ridge Associated Universities (ORAU) under DOE contract number DE-SC00014664. All opinions expressed in this paper are the author's and do not necessarily reflect the policies and views of DOE, ORAU, or ORISE. We acknowledge Yusong Bai and Jue Wang for help in SHG and PL experiments and for critical reading of this manuscript.

References

[1] G. Wang, A. Chernikov, M. M. Glazov, T. F. Heinz, X. Marie, T. Amand, and B. Urbaszek, Rev. Mod. Phys. **90**, 21001 (2018).

[2] H. Y. Yu, G. B. Liu, J. J. Tang, X. D. Xu, and W. Yao, Sci. Adv. **3**, e1701696 (2017).

[3] K. L. Seyler, P. Rivera, H. Yu, N. P. Wilson, E. L. Ray, D. G. Mandrus, J. Yan, W. Yao, and X. Xu, Nature **567**, 66 (2019).

[4] K. Tran, G. Moody, F. Wu, X. Lu, J. Choi, K. Kim, A. Rai, D. A. Sanchez, J. Quan, A. Singh, J. Embley, A. Zepeda, M. Campbell, T. Autry, T. Taniguchi, K. Watanabe, N. Lu, S. K. Banerjee, K. L. Silverman, S. Kim, E. Tutuc, L. Yang, A. H. MacDonald, and X. Li, Nature **567**, 71 (2019).

[5] P. Rivera, K. L. Seyler, H. Yu, J. R. Schaibley, J. Yan, D. G. Mandrus, W. Yao, and X. Xu, Science **351**, 688 (2016).

[6] J. Kim, C. Jin, B. Chen, H. Cai, T. Zhao, P. Lee, S. Kahn, K. Watanabe, T. Taniguchi, S. Tongay, M. F. Crommie, and F. Wang, Sci. Adv. **3**, e1700518 (2017).

[7] M. M. Fogler, L. V Butov, and K. S. Novoselov, Nat. Commun. **5**, (2014).

[8] Z. Wang, D. A. Rhodes, K. Watanabe, T. Taniguchi, J. C. Hone, J. Shan, and K. F. Mak, Nature **574**, 76 (2019).

[9] J. Wang, J. Ardelean, Y. Bai, A. Steinhoff, M. Florian, F. Jahnke, X. Xu, M. Kira, J. Hone, and X. Zhu, Sci. Adv. **5**, eaax0145 (2019).

[10] C. Jin, E. Y. Ma, O. Karni, E. C. Regan, F. Wang, and T. F. Heinz, Nat. Nanotechnol. **13**, 994 (2018).

[11] X. Hong, J. Kim, S.-F. Shi, Y. Y. Zhang, C. Jin, Y. Sun, S. Tongay, J. Wu, Y. Y. Zhang, and F. Wang, Nat. Nanotechnol. **9**, 1 (2014).

[12] F. Ceballos, M. Z. Bellus, H. Chiu, and H. Zhao, ACS Nano **8**, 12717 (2014).

[13] H. Zhu, J. Wang, Z. Gong, Y. D. Kim, J. Hone, and X.-Y. Zhu, Nano Lett. **17**, 3591 (2017).

[14] Z. Ji, H. Hong, J. Zhang, Q. Zhang, W. Huang, T. Cao, R. Qiao, C. Liu, J. Liang, C. Jin, L. Jiao, K. Shi, S. Meng, and K. Liu, ACS Nano **11**, 12020 (2017).

[15] L. A. Jauregui, A. Y. Joe, K. Pistunova, D. S. Wild, A. A. High, Y. Zhou, G. Scuri, K. De Greve, A. Sushko, C.-H. Yu, T. Taniguchi, K. Watanabe, D. J. Needleman, M. D. Lukin, H. Park, and P. Kim, Science **366**, 870 (2019).

[16] E. Y. Ma, B. Guzelturk, G. Li, L. Cao, Z.-X. Shen, A. M. Lindenberg, and T. F. Heinz, Sci. Adv. **5**, eaau0073 (2019).

[17] K. Wang, B. Huang, M. Tian, F. Ceballos, M.-W. Lin, M. Mahjouri-Samani, A. Boulesbaa, A. A. Puretzky, C. M. Rouleau, M. Yoon, H. Zhao, K. Xiao, G. Duscher, and D. B. Geohegan, ACS Nano **10**, 6612 (2016).

[18] H. Heo, J. H. Sung, S. Cha, B.-G. Jang, J.-Y. Kim, G. Jin, D. Lee, J.-H. Ahn, M.-J. Lee, J. H. Shim, H. Choi, and M.-H. Jo, Nat Commun **6**, (2015).

[19] Y. Wang, Z. Wang, W. Yao, G.-B. Liu, and H. Yu, Phys. Rev. B **95**, (2017).

[20] F. Liu, M. E. Ziffer, K. R. Hansen, J. Wang, and X. Zhu, Phys. Rev. Lett. **122**, 246803 (2019).

[21] A. G. Čabo, J. A. Miwa, S. S. Grønborg, J. M. Riley, J. C. Johannsen, C. Cacho, O. Alexander, R. T. Chapman, E. Springate, M. Grioni, J. V Lauritsen, P. D. C. King, P. Hofmann, S. Ulstrup, A. Grubis, J. A. Miwa, S. S. Grønborg, J. M. Riley, J. C. Johannsen, C. Cacho, O. Alexander, R. T. Chapman, E. Springate, M. Grioni, J. V Lauritsen, P. D. C. King, P. Hofmann, and S. Ulstrup, Nano Lett. **15**, 5883 (2015).

[22] S. Ulstrup, A. G. Čabo, D. Biswas, J. M. Riley, M. Dendzik, C. E. Sanders, M. Bianchi, C. Cacho, D. Matselyukh, R. T. Chapman, E. Springate, P. D. C. King, J. A. Miwa, and P. Hofmann, Phys. Rev. B **95**, 41405 (2017).

[23] S. Ulstrup, A. G. Čabo, J. A. Miwa, J. M. Riley, S. S. Grønborg, J. C. Johannsen, C. Cacho, O. Alexander, R. T. Chapman, E. Springate, M. Bianchi, M. Dendzik, J. V Lauritsen, P. D. C. King, and P. Hofmann, ACS Nano **10**, 6315 (2016).

[24] N. R. Wilson, P. V. Nguyen, K. Seyler, P. Rivera, A. J. Marsden, Z. P. L. Laker, G. C. Constantinescu, V. Kandyba, A. Barinov, N. D. M. Hine, X. Xu, and D. H. Cobden, Sci. Adv. **3**, e1601832 (2017).

[25] F. Liu, Q. Li, and X. -Y. Zhu, *Supplementary Information* (2020).

[26] F. Liu, W. Wu, Y. Bai, S. H. Chae, Q. Li, J. Wang, J. Hone, and X.-Y. Zhu, Science **367**, 903 (2020).

[27] M. Okada, A. Kutana, Y. Kureishi, Y. Kobayashi, Y. Saito, T. Saito, K. Watanabe, T. Taniguchi, S. Gupta, Y. Miyata, B. I. Yakobson, H. Shinohara, and R. Kitaura, ACS Nano **12**, 2498 (2018).

[28] E. Cappelluti, R. Roldán, J. A. Silva-Guillén, P. Ordejón, and F. Guinea, Phys. Rev. B **88**, 75409 (2013).

[29] Q. Zheng, W. A. Saidi, Y. Xie, Z. Lan, O. V Prezhdo, H. Petek, and J. Zhao, Nano Lett. **17**, 6435 (2017).

[30] B. Radisavljevic, a Radenovic, J. Brivio, V. Giacometti, and a Kis, Nat. Nanotechnol. **6**, 147 (2011).

[31] A. Ayari, E. Cobas, O. Ogundadegbe, and M. S. Fuhrer, J. Appl. Phys. **101**, 14507 (2007).

[32] K. F. Mak, K. He, C. Lee, G. H. Lee, J. Hone, T. F. Heinz, and J. Shan, Nat. Mater. **12**, 207 (2013).

[33] J. S. Ross, P. Rivera, J. Schaibley, E. Lee-Wong, H. Y. Yu, T. Taniguchi, K. Watanabe, J. Q. Yan, D. Mandrus, D. Cobden, W. Yao, and X. D. Xu, Nano Lett. **17**, 638 (2017).

[34] L. Waldecker, R. Bertoni, H. Hübener, T. Brumme, T. Vasileiadis, D. Zahn, A. Rubio, and R. Ernstorfer, Phys. Rev. Lett. **119**, 36803 (2017).

[35] K. F. Brennan, *The Physics of Semiconductors: With Applications to Optoelectronic Devices* (Cambridge university press, 1999).

[36] R. Wallauer, J. Reimann, N. Armbrust, J. Güdde, and U. Höfer, Appl. Phys. Lett. **109**,

162102 (2016).

[37] K. F. Mak, K. He, J. Shan, and T. F. Heinz, Nat. Nanotechnol. **7**, 494 (2012).

[38] H. Zeng, J. Dai, W. Yao, D. Xiao, and X. Cui, Nat. Nanotechnol. **7**, 490 (2012).

[39] R. Bertoni, C. W. Nicholson, L. Waldecker, H. Hübener, C. Monney, U. De Giovannini, M. Puppin, M. Hoesch, E. Springate, R. T. Chapman, C. Cacho, M. Wolf, A. Rubio, and R. Ernstorfer, Phys. Rev. Lett. **117**, 277201 (2016).

[40] A. T. Hanbicki, H. J. Chuang, M. R. Rosenberger, C. S. Hellberg, S. V Sivaram, K. M. McCreary, Mazin II, and B. T. Jonker, ACS Nano (2018).

[41] S. Ulstrup, J. C. Johannsen, F. Cilento, A. Crepaldi, J. A. Miwa, M. Zacchigna, C. Cacho, R. T. Chapman, E. Springate, F. Fromm, C. Raidel, T. Seyller, P. D. C. King, F. Parmigiani, M. Grioni, and P. Hofmann, J. Electron Spectros. Relat. Phenomena **200**, 340 (2015).

[42] S.-L. Yang, J. A. Sobota, P. S. Kirchmann, and Z.-X. Shen, Appl. Phys. A **116**, 85 (2014).

[43] M. Alonso, R. Cimino, and K. Horn, Phys. Rev. Lett. **64**, 1947 (1990).

[44] S. Tanaka, J. Electron Spectros. Relat. Phenomena **185**, 152 (2012).

[45] L.-P. Oloff, K. Hanff, A. Stange, G. Rohde, F. Diekmann, M. Bauer, and K. Rossnagel, J. Appl. Phys. **119**, 225106 (2016).

[46] H. Wang, C. Zhang, W. Chan, S. Tiwari, and F. Rana, Nat. Commun. **6**, 8831 (2015).

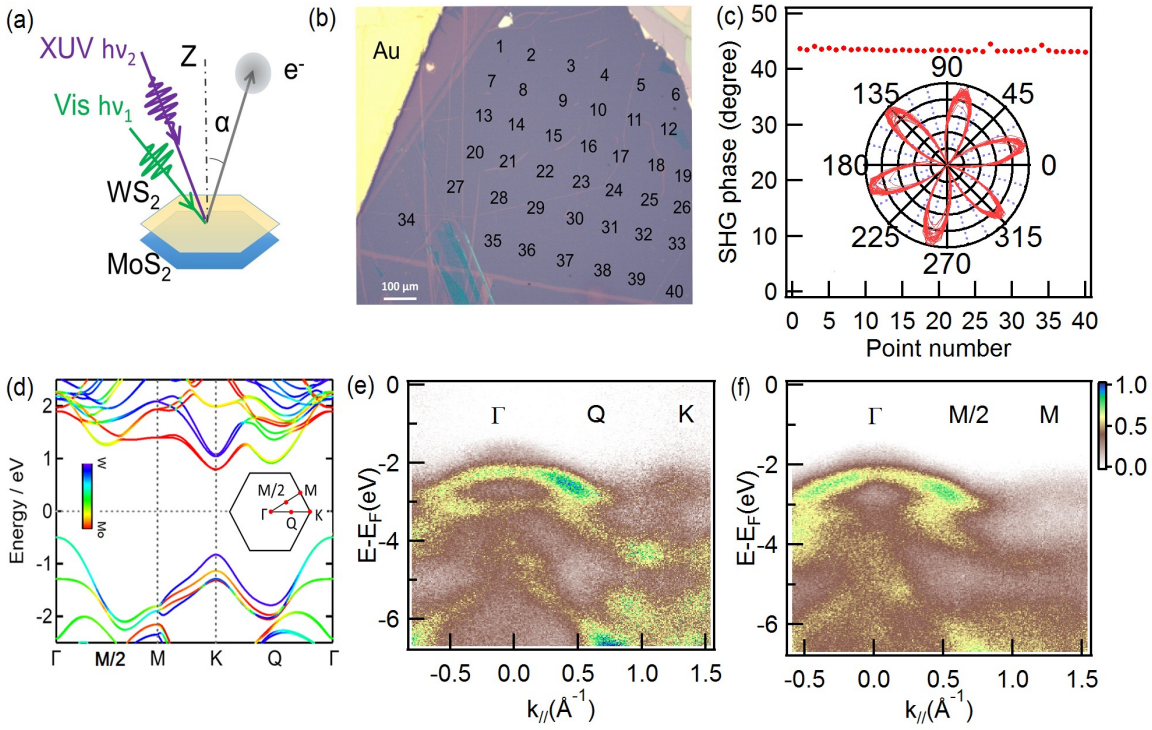

Figure 1. (a) Schematics of the TR-ARPES experiment. A femtosecond visible pulse serves as pump and the femtosecond EUV pulse is probe. The photoelectrons are detected by hemispherical analyzer at various polar angle α from surface normal for momentum resolution. (b) Image of the WS_2/MoS_2 heterostructure on 285 nm SiO_2/Si, with blue color from optical contrast. Gold electrodes are deposited on the side for grounding. A zoomed-out image of the sample is shown in Fig. S1. (c) SHG mapped across 40 different points on the mm scale heterostructure. The uniform phase indicate uniform crystal orientation. The inset is the SHG polar plot of the 40 sampled points. (d) Calculated band structure of WS_2/MoS_2 heterostructures with 0 degree alignment. (Reprinted with permission from Ref. [27]. Copyright 2018 American Chemical Society). The color scheme indicates the contribution to wavefunctions from each layer. The inset is a schematic of the different points in the Brillouin zone. (e)(f) Experimental ARPES of WS_2/MoS_2 heterostructure measured along (e) Γ-*K* direction and (f) Γ-*M* directions respectively. All TR-ARPES and ARPES measurements are performed at room temperature.

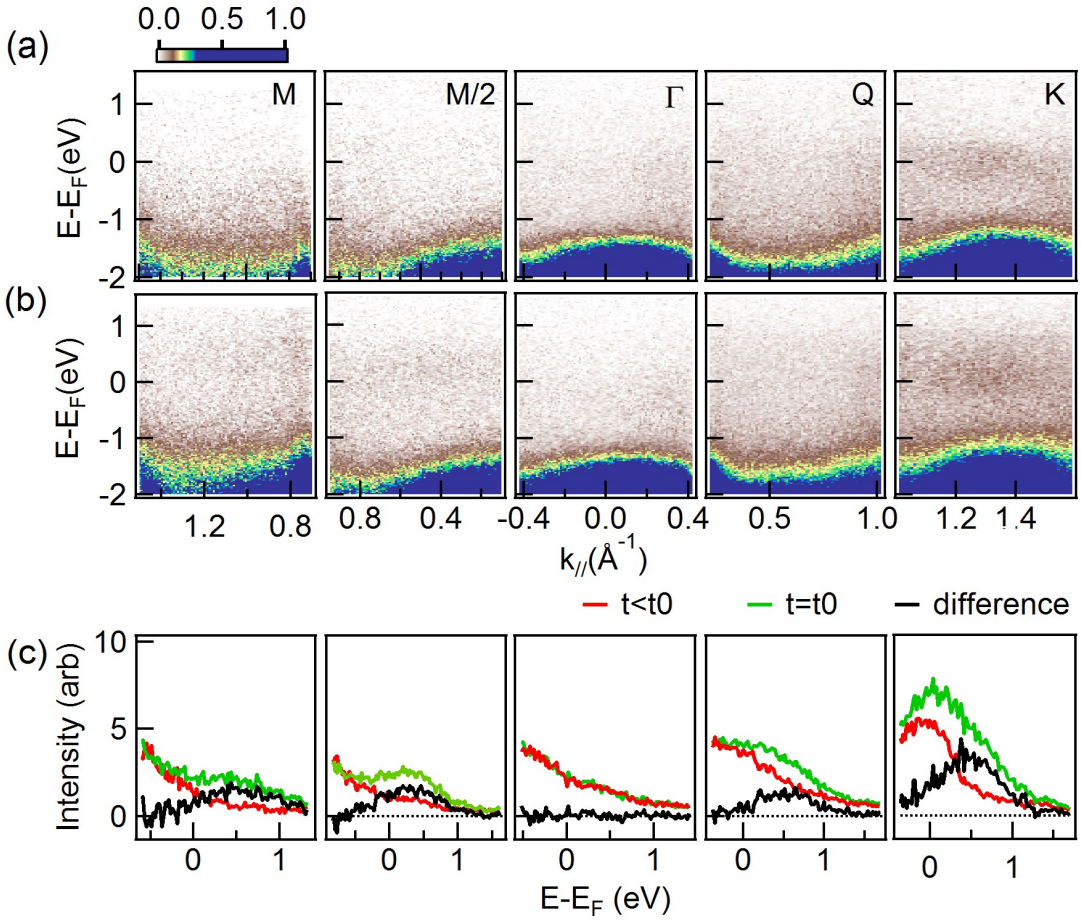

Figure 2. TR-ARPES of the WS_2/MoS_2 heterostructure (a) without ($\Delta t<0$) and (b) with ($\Delta t=0$) the visible pump excitation, respectively. The ARPES spectra are collected at *M*, *M*/2, Γ, *Q*, *K* positions in the momentum space. The color scheme is scaled up a lot to show weak signal in the CB. (c) The corresponding electron energy distribution curve (EDC) near the CB edge, collected without ($\Delta t<0$, red) and with ($\Delta t=0$, green) the visible pump excitation, and the difference with and without pump (black). The EDCs are integrated within a ±0.15 $Å^{-1}$ window of the center momentum at each point from raw photoionization signals. The visible pump is fixed at a photon energy of 2.2 eV and the probe at 22 eV. The sample is at room temperature.

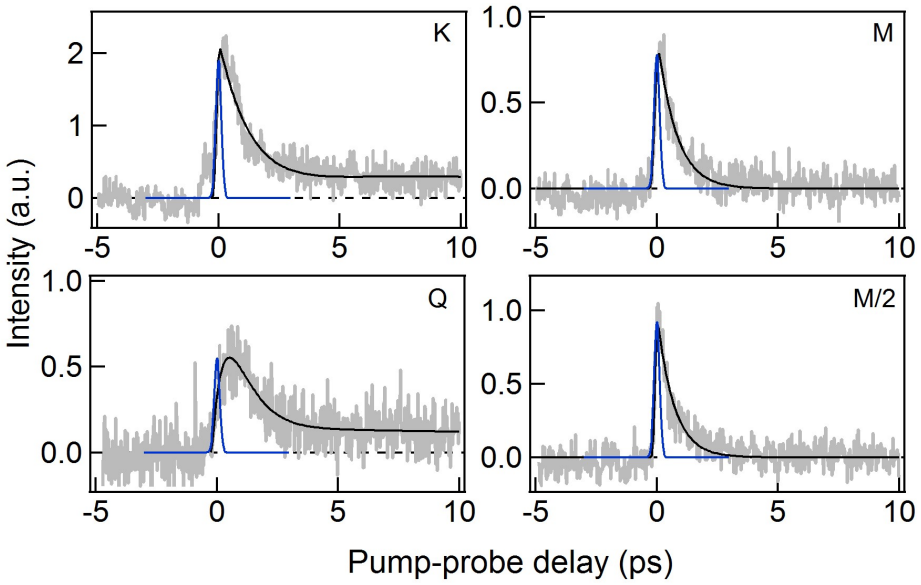

Figure 3. CB electron dynamics at *K*, *Q*, *M*/2, and *M* points as a function of pump probe delay. The integrated CB photoelectron intensities are shown as grey curves, with intensity at $\Delta t < 0$ set to zero. The solid black curves are kinetic fits and the blue curves (scaled to experimental peak intensity) are convoluted Gaussians (σ = 140 fs) representing laser pump-probe time resolution up to 70 fs ($^1/_2\ \sigma$). The dashed lines show zero intensity levels. The CB electron intensities are integrated from -0.5 eV to 2.5 eV. The corresponding TR-ARPES in 2D pseudo-color plots are shown in Fig. S5. The intensity is integrated within a ±0.15 $Å^{-1}$ window of the center momentum.

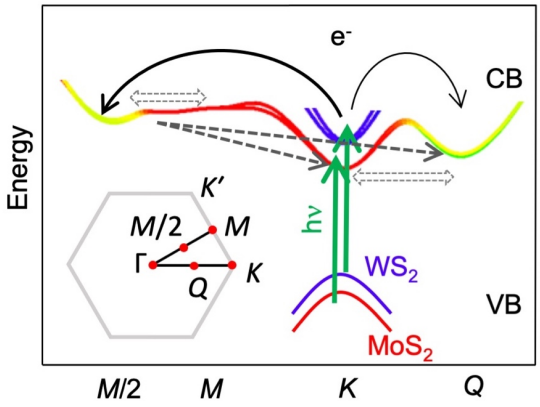

Figure 4. Schematics of intervalley electron scattering in the CB. The visible pump beam excites the electron from VB to CB in the *K* valleys (green arrows), followed by ultrafast scattering (≤ 70 fs) of electron from *K* to *M, M/2* and *Q* (black arrows). The dashed arrows represent subsequent electron scattering (~0.4 ps) from *M/2* and *M* back to *K* and *Q*. The double-ended and dashed arrows represent dynamic equilibria.